Spacer layer thickness and temperature dependence of interlayer exchange coupling in Co/Ru/Co trilayer structures

Tommy McKinnon [*], Bret Heinrich, and Erol Girt

Department of Physics, Simon Fraser University, Burnaby, British Columbia V5A 1S6, Canada

In this paper, we measure the bilinear interlayer magnetic coupling J_1 between two Co layers coupled across a Ru spacer layer over a wide range of spacer layer thicknesses from 0.4 to 3.4 nm and temperatures from 5 to 300 K. These measurements are fit using the interface-reflection interlayer magnetic coupling model in order to determine coupling strengths and electron Fermi velocities within the spacer layer in the direction perpendicular to the film interface for each of the critical spanning vectors. We find that there is a significant contribution to J_1 from several different critical spanning vectors, all with different periods of oscillation with respect to the spacer layer thickness. The results indicate that there is likely no exponential superexchangelike contribution to coupling in our samples. The nonoscillatory antiferromagnetic coupling bias of J_1 seen in thinner Ru spacer layers can be explained solely by a linear combination of oscillatory Ruderman-Kittel-Kasuya-Yosida-like coupling from several different critical spanning vectors, all with different periods of oscillation. The experimentally determined electron Fermi velocities are found to be within the range expected from theoretical calculations. The results also indicate that the interface-reflection model is capable of describing the bilinear interlayer exchange coupling in our samples over the entire range of spacer layer thicknesses and temperatures measured in this paper.

I. INTRODUCTION

Modern spintronics devices would not be possible without the discovery of oscillatory interlayer exchange coupling [1]. This is observed in thin-film structures composed of two magnetic layers coupled across a nonmagnetic spacer layer, and it oscillates between antiferromagnetic (AFC) and ferromagnetic coupling (FC) as the thickness of the spacer layer is increased [2].

This oscillatory interlayer exchange coupling allows one to engineer thin-film layer structures containing magnetic layers coupled to one another with desired coupling strengths and coupling direction (FC or AFC) as required by the application. One such spintronic application is spin transfer torque magnetic random access memory, which, at a basic level, requires two magnetic layers a free layer and a fixed layer. The direction of magnetization of the free layer is typically stable in one of two directions which are mapped to 1 and 0 to store binary information. The direction of magnetization of the fixed layer must remain fixed and not be easily rotatable. This is so that it can act as a reference and allow for reading and writing of information to the free layer.

Such a fixed layer is typically composed of a complex structure of multiple magnetic sublayers that are either FC or AFC coupled to one another [3–5]. In such a structure, the most popular spacer layer material to achieve AFC coupling is Ru(0001) because it results in strong-coupling strengths of more than -3 mJ/m^2 in sputter deposited samples [6,7].

Many theories have been created with the purpose of describing bilinear interlayer exchange coupling including Ruderman-Kittel-Kasuya-Yosida (RKKY) [8], quantum confinement [9], free electron [10–12], and interface reflection (also called quantum interference) [13,14]. For thick spacer layers, all of the theories predict the same periodicity of bilinear coupling oscillations, and the theories only differ in the prediction of the amplitude of the oscillations.

Stiles and Bruno [13,14] were able to show that the interface-reflection theory can treat metal and insulator spacers in a unified manner, which required separate theories previously. This theory also correctly predicts experimental findings, such as the dependence of coupling on the magnetic layer composition and thickness, and its temperature dependence for both conductive and insulating spacer layers. For these reasons, it appears that the interface-reflection theory is the ideal choice for predicting the physics of bilinear interlayer exchange coupling.

Previous studies comparing the various bilinear interlayer exchange coupling theories to experiment have focused on structures with magnetic layers coupled across spacer layers composed of Ag(100), Au(100), Cu(100), and Cr(100) [15]. This is because these spacer layers have relatively simple Fermi surfaces, and when coupled across these lattice planes, have only a small number of dominant so-called critical spanning vectors, resulting in relatively simple coupling oscillations that can be easily compared with theory.

On the other hand, much less comparison between theory and experiment has been performed for samples with magnetic layers coupled across transition-metal spacers (other than Cr), such as Ru(0001). This is because the Fermi surfaces are so complicated, and the number of critical spanning vectors are so large that a reliable comparison is difficult [14]. This lack of comparison makes it difficult to know how well these theories describe coupling across Ru spacer layers.

*tommy_mckinnon@sfu.ca

Additionally, most experimental studies looking at coupling across Ru(0001) spacer layers report measuring coupling oscillations that contain, or is, at least, dominated by, only one period of oscillations [16,17]. This differs from predictions from the interface-reflection theory, which Stiles [13] used to calculate that the coupling across Ru(0001) should be a superposition of several oscillatory functions with different periods of oscillations. He also showed that the magnitude of the contribution from most of these oscillatory functions are comparable to one another, which would mean that several periods of oscillation, or beating, should be seen in experiment [13].

Furthermore, coupling across Ru(0001) spacer layers has a very strong AFC bias for thinner spacer layers that might be explained by the standard RKKY-like oscillatory coupling, or it may require a superexchangelike contribution to coupling. [7,18,19]. The interface-reflection theory predicts that a nonoscillatory superexchangelike bias can occur for thin spacer layers if evanescent electron states are contributing to the coupling. This could account for an AFC bias of coupling that decreases exponentially with the thickness of the spacer layer [14].

In this paper, we measure the bilinear interlayer exchange coupling between two Co layers coupled across a Ru(0001) spacer layer over a wide range of spacer layer thicknesses from 0.4 to 3.4 nm using a vibrating sample magnetometer (VSM). We then fit the data with the interface-reflection model that includes a superexchangelike contribution from evanescent states. From this fit, we determine if the interface-reflection model accurately describes coupling in our samples, and whether there is a superexchangelike contribution.

The interface-reflection model predicts that any superexchangelike contribution to bilinear interlayer exchange coupling caused by evanescent states will result in a coupling strength that increases with increasing temperature. This is opposed to RKKY-like oscillating coupling, which has the opposite temperature dependence. This has also been verified by experiment [20]. This superexchangelike coupling strength is predicted to decrease in magnitude exponentially with the spacer layer thickness, meaning that it would be most prevalent for the thinner spacer layers. Thus, if there is a superexchangelike contribution to coupling, we would expect to see a temperature dependence of the coupling strength that increases with increasing temperature for the thinnest spacer layers.

Therefore, to confirm the existence of a superexchangelike contribution to coupling, or lack thereof, we investigate the J_1 temperature dependence in our thinner spacer layer samples with spacer layer thicknesses from 0.4 to 1 nm and a temperature range of 5 to 300 K. We then fit these data using the interface-reflection model.

II. THEORY

A. Interlayer exchange-coupling energy

The interlayer exchange-coupling energy U_{coupling} describes the exchange interaction that occurs between two magnetic thin films separated by a nonmagnetic spacer layer. The coupling energy per unit area between the magnetic thin-film interfaces separated by a nonmagnetic spacer layer is given by [21,22]

$$U_{\text{coupling},1} = -J_1 \frac{\boldsymbol{M}_1 \cdot \boldsymbol{M}_2}{M_{s,1}M_{s,2}} + J_2 \left(\frac{\boldsymbol{M}_1 \cdot \boldsymbol{M}_2}{M_{s,1}M_{s,2}}\right)^2, \quad (1)$$

where J_1 and J_2 are the bilinear and biquadratic coupling terms, respectively, the 1 and 2 subscripts correspond to each of the two coupled magnetic layers, $\boldsymbol{M}_i$ is the magnetization of layer i, $M_{s,i} = |\boldsymbol{M}_i|$ as is the case for ferromagnetic materials, which is what is studied in this paper. The bilinear term favors parallel (positive J_1) or antiparallel (negative J_1) alignment of the separated magnetic layers. The biquadratic term can only be positive and favors $90°$ alignment of the separated magnetic layers. This paper will focus on the physics of the bilinear term.

B. Bilinear interlayer exchange-coupling model

We will be using a model based on the interface-reflection theory as described by Stiles and Bruno [13,14]. This model considers the magnetic/spacer/magnetic trilayer structure as a quantum well where the magnetic layers are the walls of the well, and the spacer layer is the well itself. Interlayer exchange coupling is caused by the electron states that exist within the spacer layer material that reflect from the walls of the well. The electron states that contribute to the coupling oscillations are determined by the critical spanning vectors from the Fermi surface of the spacer layer material. Critical spanning vectors, which are shown for Ru(0001), in Fig. 3, are vectors in the direction of the interface normal, that connect two sheets of the Fermi surface that are parallel to each other at the end points of the vector.

The interface-reflection model predicts that the coupling term J_1 has the form [13,14]

$$J_1(d) = \text{Im} \sum_{\alpha} \frac{J^\alpha}{d^2} e^{i(q_\perp^\alpha d + \phi^\alpha)}, \quad (2)$$

where it is summing over contributions from different electron states within the spacer layer, corresponding to each critical spanning vector, labeled by α. d is the thickness of the spacer layer, J^α is the coupling strength of the electron state, $q_\perp^\alpha$ is the critical spanning vector, and ϕ^α is the phase of the electron probability density after scattering from a wall of the quantum well. Phase ϕ^α of each state α is defined by the topology of the Fermi surface of the spacer layer at the end points of its critical spanning vector $q_\perp^\alpha$. For thick spacer layers, ϕ^α is equal to 0, $\pi/2$, and π when the Fermi surface at this location is a minimum, a saddle point, and a maximum, respectively [8].

J^α is equal to [13,14]

$$J^\alpha = -\left[\frac{\hbar}{2\pi^2}\kappa^\alpha v_\perp^\alpha\right][|R_\uparrow^\uparrow|^2 + |R_\downarrow^\uparrow|^2 - 2|R_\uparrow^\uparrow R_\downarrow^\uparrow|]F^\alpha(d, T),$$

$$(3)$$

where κ^α is the radius of curvature of the Fermi surface of the spacer layer material and $v_\perp^\alpha$ is the electron state velocity within the spacer layer material in the direction perpendicular to the magnetic/spacer interface, both calculated at the location of the end points of the critical spanning vectors. $R_\uparrow^\uparrow$ ($R_\downarrow^\uparrow$) is the reflection amplitude for a spin-up (spin-down) electron

reflecting from the energy barrier formed when both magnetic layers have magnetization parallel with one another in the up direction.

$F^\alpha(d, T)$ in Eq. (3) is the temperature dependence, which is given by [23–25]

$$F^\alpha(d, T) = \frac{x^\alpha}{\sinh x^\alpha}, \tag{4}$$

where

$$x^\alpha = 2\pi k_B T \left[\frac{d}{\hbar v_\perp^\alpha} + D_\phi^\alpha \right], \tag{5}$$

where k_B is Boltzmann's constant and $\hbar$ is the reduced Planck's constant. The first term in the square brackets is the temperature-dependence contribution from the spacer layer, and D_ϕ^α is the temperature-dependence contribution from the interface reflections on either side of the spacer layer. This first term arises due to the fact that at finite temperatures, the Fermi surface and critical spanning vectors are broadened. This results in a distribution of critical spanning vectors with slightly different lengths, which smooths out the J_1 oscillations, leading to a reduction in their magnitude.

The second term, to first order, is equal to the derivative of the phase shift caused by the reflection of electrons at the interfaces with respect to energy $D_\phi^\alpha = \frac{d\phi^\alpha}{dE}$ [23–25]. Like before, finite temperature broadens the Fermi surface, resulting in coupling electron states with a distribution of energies. If $\frac{d\phi^\alpha}{dE}$ is large, this distribution of coupling electron states will have relatively large distribution in their phase. When added together, this results in a smearing of the J_1 oscillations, leading to a reduction in their magnitude.

For thicker spacer layers, the first term in Eq. (5), which depends on d, becomes larger, making the second interface term insignificant. Thus, for thicker spacer layers, one can approximate the temperature dependence with only the first spacer layer term. However, in our case, the spacer layers are thin enough that the two terms are of comparable magnitude and must both be included.

It must be noted that this model is only exact in the limit of infinitely thick spacer layers. However, it has been shown to be reasonably accurate for thicknesses greater than one period of J_1 oscillations [13]. Thus, we expect that when J_1 measurements are fit using this model, the fit will be less accurate for the measurements of the thinnest spacer layers.

C. Evanescent states

The interface-reflection model is able to describe coupling across metallic and insulating spacer layers [14]. The only difference is that the electron states contributing to coupling have oscillatory wave functions for the metallic case and exponentially decaying tunneling wave functions for the insulating case. In the latter case, the critical spanning vector $q_\perp^\alpha$ in Eq. (2) will be imaginary instead of real. This will result in J_1 that decreases exponentially with spacer layer thickness rather than being oscillatory.

In a crystal, the allowed states are Bloch waves,

$$\psi(r) = u(r)e^{ikr}, \tag{6}$$

where $u(r)$ is a periodic function with the periodicity of the crystal lattice. This holds true for any complex wave vector [26]. For bulk crystals, states with imaginary wave vectors cannot exist because they increase exponentially to infinity and cannot be normalized. However, for finite systems, such as the spacer layer here, the wave function is limited in space and does not go to infinity. This allows states with imaginary wave vectors to exist. Therefore, just like insulating layers, metallic spacer layers can also have evanescent electron states that contribute to coupling. Since these decay exponentially, their contribution will be significantly smaller than that of the real wave vectors and are usually ignored. However, we will be measuring coupling across spacer layers as thin as 0.4 nm, so there is a possibility for these to contribute.

If the wave vector is real, Eq. (2) becomes [13,14]

$$J_1(d) = \sum_\alpha \frac{J^\alpha}{d^2} \sin(q_\perp^\alpha d + \phi^\alpha), \tag{7}$$

and if the wave vector is imaginary, Eq. (2) becomes [13,14,27]

$$J_1(d) = \sum_\alpha \frac{J^\alpha}{d^2} e^{i\phi^\alpha} e^{-d/\delta_\perp^\alpha}, \tag{8}$$

where $\delta_\perp^\alpha = 1/\text{Im}(q_\perp^\alpha)$ is the decay length and the term $e^{i\phi^\alpha}$ determines whether the exponential favors ferromagnetic or antiferromagnetic coupling where ϕ^α is no longer constrained to the range of 0-π in the case of evanescent states, so this term can be positive or negative [14,27].

One useful difference between coupling caused by electron states with real and imaginary wave vectors is that they have opposite temperature dependence. This can be seen easily using the following relation:

$$\frac{ix}{\sinh ix} = \frac{x}{\sin x}, \tag{9}$$

which, along with the fact that if the wave vector is imaginary, its velocity will be as well, is the same form as the temperature dependence in Eq. (4). The different dependence of J_1 for oscillating and evanescent wave functions is shown in Fig. 1. The opposite dependence allows for the determination of which case is contributing to coupling by measuring the temperature dependence of J_1 in a sample. It should be noted that each term, in the sum in Eq. (2), has its own temperature dependence. Depending on the spacer layer thickness and critical spanning vector, the zero-temperature J_1 could be positive for some terms and negative for others. Since the measured temperature dependence is the sum of all terms, this can also lead to opposite temperature dependence than expected. Therefore, in order to compare the model to experiment we need to consider the sum of the individual temperature dependence of each critical spanning vector.

D. Critical spanning vectors for the Ru spacer layer

In order to use the interface-reflection model as described by Eq. (2), we first need to determine the critical spanning vectors $q_\perp^\alpha$ for the spacer layer, which is Ru textured in the [0001] direction in our case. In order to have the most accurate values, we have determined the critical spanning vectors from
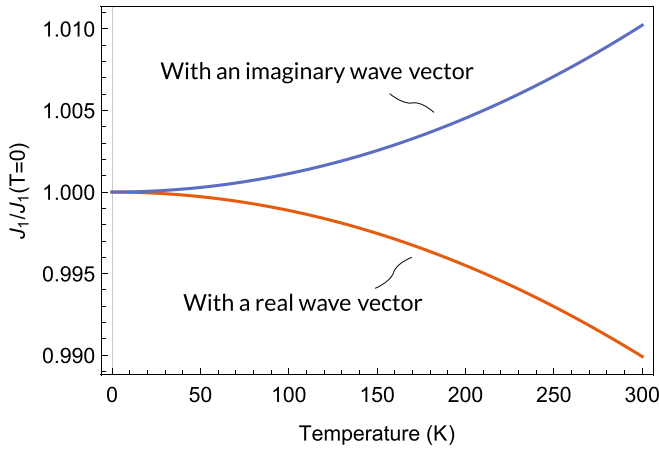
FIG. 1. The temperature dependence of J_1 when the critical spanning vector is real using Eq. (4) with $d = 0.4$ nm, $v_\perp^\alpha = 4 \times 10^5$ m/s, $D_\phi^\alpha = 0$ J^{-1} (orange) or imaginary with $d = 0.4$ nm, $v_\perp^\alpha = i4 \times 10^5$ m/s, $D_\phi^\alpha = 0$ J^{-1} (blue).

experimental measurements of the Ru Fermi surface from Refs. [28,29].

It is important to note that the critical spanning vectors we are using are for bulk Ru. The Fermi surface of very thin spacer layers may differ from that of bulk due to lattice strain or other effects. However, as we show later in this paper, these bulk critical spanning vectors appear to work quite well even for thinner spacer layers, at least, for the Co/Ru(0001)/Co trilayer structure that we are studying.

A selection of the critical spanning vectors for bulk Ru in the [0001] direction are shown in Fig. 3 superimposed on top of two mirrored slices of the Fermi-surface diagram, labeled from a to h. The Fermi-surface diagram is based on one from Ref. [29] that was calculated using the linear-muffin-tin-orbital method (LMTO) and fit to experimentally determined sheet radii obtained through de Haas–van Alphen measurements in Ref. [28]. The labeled high-symmetry points in the Fermi-surface diagram correspond to locations in the Brillouin zone for Ru as shown in Fig. 2. The critical spanning vector lengths, along with their phase shifts ϕ^α are also shown in Table I. Labels denoted with * are approximated
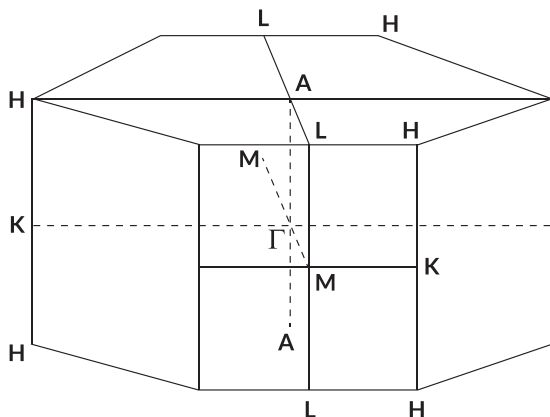
FIG. 2. The Brillouin zone for hexagonal close-packed Ru with relevant high-symmetry points labeled.
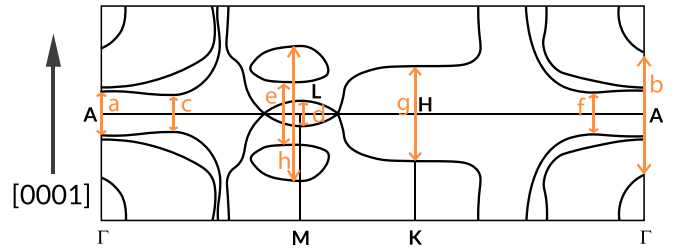
FIG. 3. A selection of single-sheet critical spanning vectors for a Ru spacer layer in the [0001] direction. The orange arrows labeled a–h are the critical spanning vectors. The vectors are superimposed on top of two mirrored Ru Fermi-surface diagrams based on one from Ref. [29], which have been created using the LMTO method and fit to experimentally determined sheet radii obtained through de Haas–van Alphen measurements in Ref. [28]. The high-symmetry points of the Brillouin zone are also labeled and correspond to points shown in Fig. 2. The values for these vectors can be found in Table I.

from the LMTO Fermi-surface fit to de Haas–van Alphen measurements, whereas the others are obtained directly from de Haas–van Alphen measurements.

Critical spanning vectors that correspond to evanescent states cannot be measured experimentally in bulk material. They have been measured in finite systems, such as photonic crystals [30], however, those are for different materials than we are studying here. As such, the only way to determine the evanescent state critical spanning vectors is to simulate the complex Fermi surface with methods, such as the LMTO method, which is known to be only approximately correct without fitting to experimental results. The complex Fermi-surface sheets are also very intricate and numerous, leading to a large number of imaginary critical spanning vectors [14]. Thus, instead of calculating the expected decay lengths of any imaginary critical spanning vectors, we will leave the decay lengths as fitting parameters and allow the fit to J_1 measurements to determine the appropriate decay lengths.

TABLE I. A selection of single-sheet critical spanning vectors and phase shifts for a Ru spacer layer in the [0001] direction corresponding to the labeled vectors in Fig. 3. All of the $q_\perp^\alpha$ values were obtained from Refs. [28,29] where they measured the values experimentally as determined by the de Haas–van Alphen effect. Labels denoted with * are approximated from the LMTO Fermi-surface fit to de Haas–van Alphen measurements, whereas the others are obtained directly from de Haas–van Alphen measurements. Note, these critical spanning vectors are for bulk Ru.

Label	$q_\perp^\alpha$ (nm^{-1})	ϕ^α (rad)
a_1^*	3.01	π
a_2^*	2.54	$\pi/2$
b	9.21	π
c^*	1.61	π
d^*	1.86	0
e	3.77	π
f^*	2.08	$\pi/2$
g^*	6.89	π
h^*	9.43	0

FIG. 4. $J_1(d)$ for a single critical spanning vector as determined by Eq. (2) with $q_\perp^\alpha = 9$ nm^{-1}, $J^\alpha = 1$ mJ/m^2, $v_\perp^\alpha = 8 \times 10^5$ m/s, $D_\phi^\alpha = 2 \times 10^{19}$ J^{-1}. The orange line is assuming a constant J^α, and the dashed blue line uses a J^α that depends on the spacer layer thickness due to $F^\alpha(d, T)$ at 298 K.

If there are any imaginary critical spanning vectors in Ru(0001), the exponentially decreasing contribution to J_1 means that one with the largest decay length will dominate. Thus, we have chosen to approximate the sum of any possible imaginary critical spanning vectors with a single exponentially decaying term. For other metallic spacer layers with simpler Fermi surfaces, such as Cu, Ag, and Au, most of the imaginary critical spanning vectors, if any, have decay lengths between 0.2 and 0.5 nm [14]. Therefore, we have chosen to limit the range of the decay length fitting parameter to between 0.1 and 1 nm and allow the fit to determine exactly which decay length fits the data best. This term has the form

$$J_1(d) = \frac{J^\alpha}{d^2} e^{-d/\delta_\perp^\alpha}, \qquad (10)$$

where we constrain 0.1 nm $< \delta_\perp^\alpha <$ 1 nm and we have also assumed $e^{i\phi^\alpha} = -1$ because the purpose of this nonoscillatory term is to account for AFC bias seen when coupling is across thin Ru(0001) spacer layers.

The interface-reflection interlayer exchange-coupling model [13,14] only takes into account critical spanning vectors within the same sheet. So, we have not included any critical spanning vectors between two different sheets.

E. Fitting for room-temperature J^α values

We first fit room-temperature J_1 vs d measurements using Eq. (2) with the real and imaginary critical spanning vectors from Sec. II D in order to determine J^α for each critical spanning vector. From this fit, we also determine if there is a contribution to coupling from evanescent states. In order to simplify this particular fit and avoid overfitting, we perform the approximation that J^α does not depend on the thickness of the spacer layer. At finite temperatures, J^α does have a slight dependence on the thickness of the spacer layer as can be seen in Eq. (5). However, this dependence is insignificant compared to $1/d^2$ in Eq. (2) and, therefore, can be neglected. Figure 4 shows the accuracy of this approximation for J_1 for

a single critical spanning vector with $q_\perp^\alpha = 9$ nm^{-1}, $J^\alpha = 1$ mJ/m^2, $v_\perp^\alpha = 8 \times 10^5$ m/s, $D_\phi^\alpha = 2 \times 10^{19}$ J^{-1}. These are all typical values for critical spanning vectors for a Ru(0001) spacer layer. It can be seen that this approximation is fairly accurate.

F. Fitting J_1 temperature-dependence measurements

At zero temperature, $F^\alpha(d, T = 0$ K$) = 1$, then as temperature increases, $F^\alpha(d, T)$ becomes larger or smaller. The effect of this is to scale J^α from its zero-temperature value, and as a result, modify the critical spanning vector's contribution to J_1. Because of this, the temperature dependence of each term in Eq. (2) can be rewritten as the temperature dependence multiplied by the zero-temperature coupling strength,

$$J_1(d, T) = \sum_\alpha J_1^\alpha(d, T = 0 \text{ K})F^\alpha(d, T), \qquad (11)$$

where

$$J_1^\alpha(d, T) = \text{Im}\frac{J^\alpha(d, T)}{d^2} e^{i(q_\perp^\alpha d + \phi^\alpha)}, \qquad (12)$$

which is just an individual term from within the sum in Eq. (2), and we have explicitly showed that $J^\alpha(d, T)$, given by Eq. (3), is a function of the spacer layer thickness and temperature, and $F^\alpha(d, T)$ is given by (4). Because of the oscillatory or exponential contribution to $J_1^\alpha(d, T)$, the weighting of the temperature dependence of each term will change in magnitude relative to one another depending on the spacer layer thickness.

The contributions from any evanescent states are exponentially decreasing functions, and they will dominate for thinner spacer layers. Therefore, if they exist, we would expect J_1 to increase with temperature for thinner spacer layers, similar to the blue line in Fig. 1.

In order to determine $J_1^\alpha(d, T = 0$ K$)$ for use in Eq. (11), we use the bulk Ru $q_\perp^\alpha$ values from Table I and the J^α values obtained from the fit of room-temperature J_1 data. With these, we can calculate the room-temperature $J_1^\alpha(d, T = 298$ K$)$ for each critical spanning vector. This is related to the zero-temperature $J_1^\alpha(d, T = 0$ K$)$ by the relation $J_1^\alpha(d, T = 298$ K$) = J_1^\alpha(d, T = 0$ K$)F^\alpha(d, T = 298$ K$)$. Thus, we can determine $J_1^\alpha(d, T = 0$ K$)$ by

$$J_1^\alpha(d, T = 0 \text{ K}) = \frac{J_1^\alpha(d, T = 298 \text{ K})}{F^\alpha(d, T = 298 \text{ K})}. \qquad (13)$$

Additionally, instead of fitting the absolute temperature dependence, we fit the ratio $J_1(d, T)/J_1(d, T = 0$ K$)$. Considering all of this, our temperature-dependence fitting function that we use is given by

$$\frac{J_1(d, T)}{J_1(d, T = 0 \text{ K})} = \frac{\sum_\alpha \dfrac{J_1^\alpha(d, T = 298 \text{ K})}{F^\alpha(d, T = 298 \text{ K})} F^\alpha(d, T)}{J_1(d, T = 0 \text{ K})}. \qquad (14)$$

Our fitting procedure is as follows: We first fit the room-temperature J_1 data as explained above and then use the obtained results to determine $J_1^\alpha(d, T = 298$ K$)$ for each critical spanning vector. Next, we plug those into Eq. (14) and then use this equation to simultaneously fit the temperature dependence of J_1 for several samples with different Ru spacer
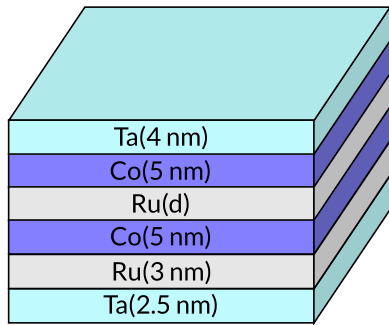
FIG. 5. The thin-film structure of the series of samples sputtered and studied in this paper. The thickness of the spacer layer d is varied from 0.4 to 3.4 nm.

FIG. 6. Coupling strength J_1 as a function of the thickness of the Ru spacer layer for our Co/Ru/Co series of samples, blue circles, and the Pt/Co/Ru/Co samples from Girt and Richter [32], orange triangles.

layer thicknesses. In these temperature-dependence fits, the only fitting parameters will be $v_\perp^\alpha$ and D_ϕ^α as shown in Eq. (5).

III. EXPERIMENTAL

We have sputtered a series of samples with the structure Ta(2.5 nm)/Ru(3 nm)/Co(5 nm)/Ru(d)/Co(5 nm)/Ta(4 nm), where d is the Ru spacer layer thickness and is varied from 0.4 to 3.4 nm. The structure of this sample can be seen in Fig. 5. For brevity, this series of samples will be referred to as the Co/Ru/Co series. The Co and Ru thin films are textured in the [0001] direction as confirmed by x-ray diffraction measurements.

All samples are deposited by means of rf magnetron sputtering on oxidized Si substrates. The deposition conditions and sample preparation are explained in detail in our previous work [31]. The demagnetizing dipolar fields in the two magnetic layers are much larger than any fields perpendicular to the film that arise from the surface and magnetocrystalline anisotropies, forcing the magnetization to lie in plane. The samples are polycrystalline, and rotated during deposition, resulting in the in-plane magnetocrystalline anisotropy being averaged out causing the easy plane of the magnetic anisotropy being on the plane of the sample. The samples are also capped with 4 nm of Ta to protect the top magnetic layer from oxidation or water absorption from the atmosphere.

The technique we use to determine J_1 within our samples only works if the two magnetic layers are not FC coupled. There are some regions of spacer layer thickness where coupling is FC, which we are unable to measure. As such, we have decided to also include previously obtained data for the FC regions from Girt and Richter Ref. [32] for J_1 measurements in samples with the structure $12 \times$ [Co(0.25 nm)/Pt(0.9 nm)]/Co(1 nm)/Ru(d)/Co(1 nm)/$4 \times$ [Pt(0.9 nm)/CoCr(0.25 nm)] where the parts in square brackets are multilayers. This series of samples will be referred to as the Pt/Co/Ru/Co series. In this case, J_1 is the coupling strength of the two Co layers across the second Ru layer, which has a thickness d, which is varied from 1.07 to 2.82 nm. Since the Co layer is grown on top of Pt instead of Ru, it is possible that it has a strained lattice that is slightly different than is the case for our samples. In order to determine if this has a significant effect on coupling oscillations, we have plotted our data along with data from
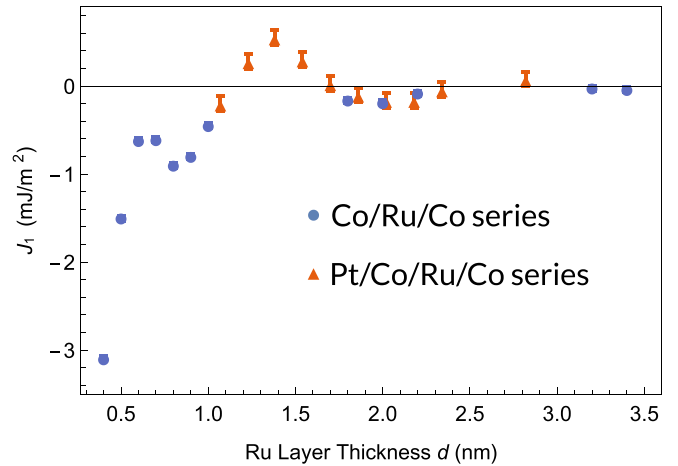
Girt and Richter [32] in Fig. 6 where we can compare measurements for overlapping data. The blue circles are the Co/Ru/Co series data, whereas the orange triangles are the Pt/Co/Ru/Co series data. It can be seen that the data from the two different series of samples seem to differ only slightly in the range from 1.7 to 2.3 nm. We have also confirmed that Co/Ru/Co series samples with Ru layer thicknesses of 1.6, 2.4, 2.8, and 3.0 nm are all FC coupled, which is in agreement with data for the Pt/Co/Ru/Co series. Thus, by increasing the size of the error bars of the Pt/Co/Ru/Co data, both series are in agreement within the uncertainty. Additionally, we only use the Pt/Co/Ru/Co data within the range of the first FC peak for spacer layer thicknesses from 1.1 to 1.7 nm.

With this combination of data from the Co/Ru/Co series and Pt/Co/Ru/Co series, we are able to fit the coupling model to data over a wider range of spacer layer thicknesses to better evaluate its accuracy.

J_1 in our samples is determined by measuring $M(H_{dc})$ (magnetization as a function of applied external field), where H_{dc} is the applied external field using VSM and then fitting the measurements using our micromagnetics model. Details of this model can be found in Refs. [33,34]. An example of a typical $M(H_{dc})$ measurement using VSM (blue points) along with a fit using our micromagnetics model (orange line) is shown in Fig. 7. The sample measured is one from the Co/Ru/Co series with a Ru spacer layer thickness of 0.4 nm. The sample temperature during the measurement was 300 K. The parameters obtained from the fit are $J_1 = -3.60 \pm 0.01$, $J_2 = 0.19 \pm 0.01$ mJ/m^2, and so-called exchange stiffness $A_{ex} = 1.7 \pm 0.1 \times 10^{-11}$ J/m.

The low-temperature measurements were performed with the same VSM tool. We found that the M_s of Co did not change significantly within the temperature range we tested. This is expected considering its Curie temperature is 1400 K [35].

For the purpose of normalizing our J_1 measurements to zero temperature, we have assumed that the J_1 obtained from fitting 5-K data is equal to that of 0-K data. This is an
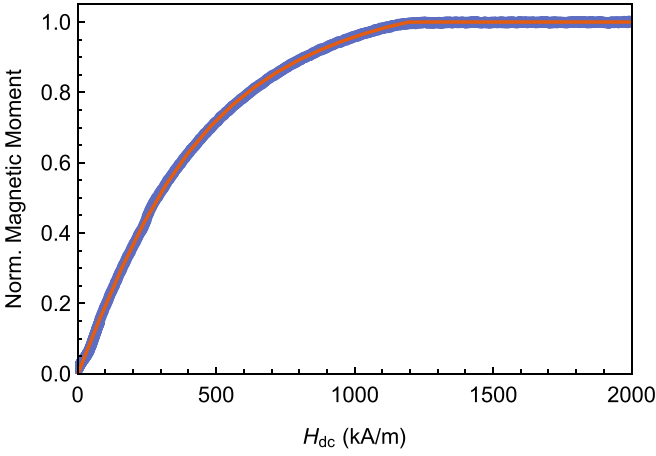
FIG. 7. Example of typical $M(H_{dc})$ data obtained using VSM (blue points) along with a fit using our micromagnetics model (orange line) [33,34]. The sample measured is one from the Co/Ru/Co series with a Ru spacer layer thickness of 0.4 nm. The sample temperature during the measurement was 300 K. The parameters obtained from the fit are $J_1 = -3.60 \pm 0.01$ mJ/m^2, $J_2 = 0.19 \pm 0.01$ mJ/m^2, and exchange stiffness $A_{ex} = 1.7 \pm 0.1 \times$ J/m, $M_s = 1350 \pm 10$ kA/m.

accurate assumption because the slope of $F(d, T)$ near $0°$ is approximately zero.

IV. RESULTS AND DISCUSSION

The J_1 coupling strength measurements for the combined Co/Ru/Co and Pt/Co/Ru/Co series are shown in Fig. 8. The orange line fit was obtained using Eq. (2) with the critical spanning vectors listed in Table I along with an additional
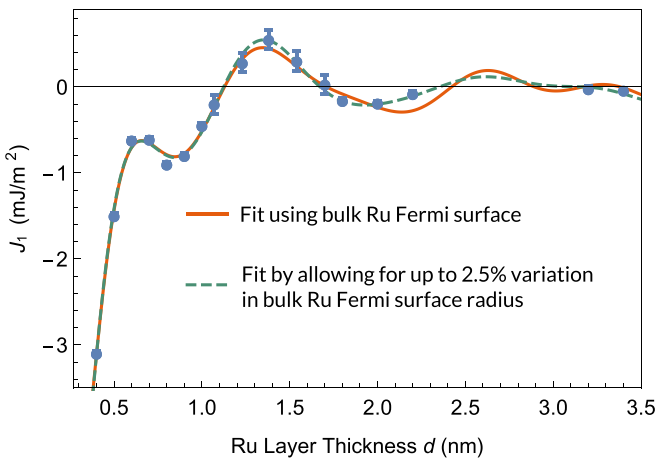
FIG. 8. Coupling strength J_1 as a function of the thickness of the Ru spacer layer for the combined Co/Ru/Co and Pt/Co/Ru/Co series of samples. The blue points are experimental data. The orange line is the fit with Eq. (2) using critical spanning vectors from Table I. The dashed green line is the fit using the same equation and critical spanning vectors, except now the lengths of the critical spanning vectors are allowed to vary in length corresponding to up to 2.5% in the Fermi-surface sheet radius.
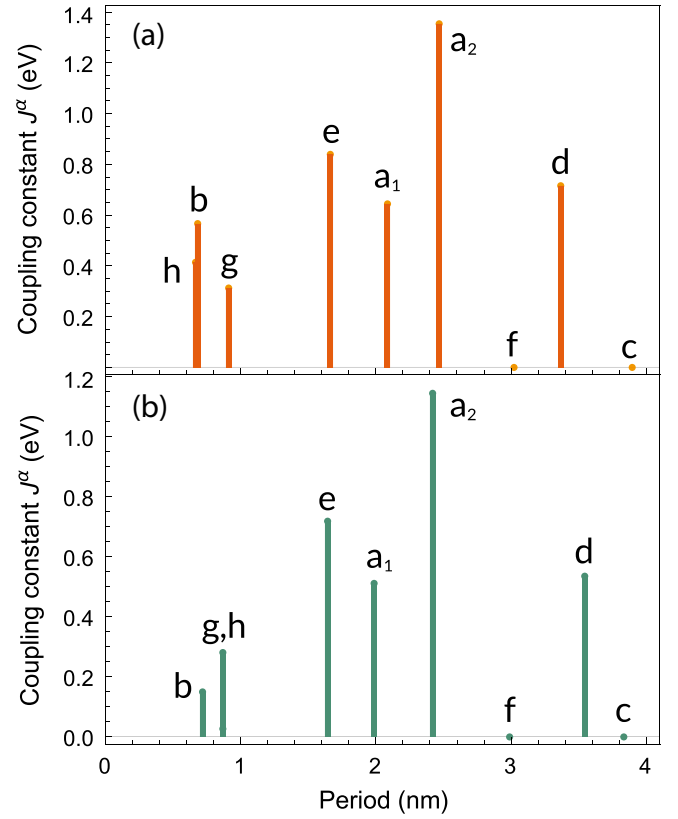
FIG. 9. J^α values with corresponding periods of oscillation ($2\pi/q_\perp^\alpha$) obtained from fitting the J_1 measurements in Fig. 8 with Eq. (2) using (a) the bulk Ru critical spanning vectors shown in Table I, and (b) modified critical spanning vectors allowing up to 2.5% change in the Fermi-surface sheet radius. Each J^α is labeled with the corresponding critical spanning vector from Table I.

imaginary critical spanning vector corresponding to an exponentially decaying nonoscillating contribution to J_1.

The coupling strengths of each critical spanning vector J^α obtained from both fits are shown in Fig. 9.

The fit shown in Fig. 8 has resulted in fitting parameters for the exponentially decaying contribution as shown in Eq. (10 of a decay length of 0.35 nm with a weight of $J^\alpha = 1 \times 10^{-5}$ eV. This coupling strength from a possible imaginary critical spanning vector is five orders of magnitude smaller than the J^α values from real critical spanning vectors as shown in Fig. 9. This indicates that there is likely no exponentially decaying superexchangelike contribution to J_1 from evanescent electron states in the samples measured.

The coupling strengths in Fig. 9(a) show that all but two of the critical spanning vectors have a significant contribution to the overall interlayer exchange coupling. This finding is in qualitative agreement with the predictions made by Stiles [13], which predicted significant contributions from wide distribution of critical spanning vectors as opposed to being dominated by one or two. It should be noted that the periods of oscillation for each of the critical spanning vectors in this paper differ slightly from that of Stiles [13] because they approximated them using the local-density approximation theoretical method, whereas we used values from experiment.

It is remarkable how accurate this fit is considering that the model is only exact for very thick spacer layers. Additionally, we have used the critical spanning vectors obtained from the Fermi surface of bulk Ru. On the thin end of the series, the Ru spacer layer is only a few atomic layers thick. The 8% lattice mismatch between Co and Ru on the (0001) plane is very likely to compress the Ru crystallographic unit cell on the plane and expand it along the c axis. This will result in a modification of the Fermi surface, causing it to deviate significantly from that of bulk Ru. It will also result in a change in the size of the Brillouin zone. Both of these factors could result in critical spanning vectors that deviate from those obtained from bulk Ru.

To account for these two factors, we have added an additional fit to the data, shown as a dashed green line in Fig. 8. This fit is the same as that of the orange line, except that now an additional fitting parameter has been added for each critical spanning vector, allowing the length to be scaled in the form $q_\perp^{\alpha'} = C q_\perp^\alpha$, where $q_\perp^{\alpha'}$ is the new critical spanning vector, C ranges from 0.95 to 1.05, which corresponds to a maximum of a 2.5% change in the perpendicular component of the radius of the Fermi-surface sheet. This additional fitting parameter can take into account small changes in the Fermi surface that is expected for the samples studied. It can be seen that by making this change, the fit is improved significantly, going through almost all data points. However, it should be noted that the additional fitting parameters that allow for a small variation in the Fermi-surface radius increases the chance of overfitting. Therefore, this result only serves as an indication that there might be the potential to improve the fit further by taking into account differences in the Fermi surface for thinner films as compared to the bulk. The J^α values obtained from this new fit are shown in Fig. 9(b). It can be seen that the period of oscillation of the new $q_\perp^{\alpha'}$ critical spanning vectors differ only slightly from those obtained from the Fermi surface of bulk Ru as shown in Fig. 9(a).

For the remaining temperature-dependence results, the critical spanning vectors of bulk Ru with the unmodified Fermi surface are used. Additionally, the critical spanning vectors labeled as f and c, which have $J^\alpha = 7.2 \times 10^{-6}$ and $J^\alpha = 6.0 \times 10^{-6}$ eV, respectively, are approximately equal to zero and, therefore, will not contribute significantly to the temperature dependence. Because of this, they are set to 0 and ignored for the remaining temperature-dependence results.

Figure 10 shows the J_1 temperature dependence for the Co/Ru/Co series with spacer layer thickness ranging from 0.4 to 1 nm and temperatures from 5 to 300 K, normalized to the zero-temperature J_1. The circles are experimental data, and the lines are a single simultaneous fit using Eq. (14). This fit uses the J^α values determined from fitting the room-temperature data in Fig. 8. However, as previously discussed, that fit resulted in $J^\alpha = 1 \times 10^{-5}$ eV for the exponentially decaying evanescent state contribution, which is much smaller than that of the real critical spanning vector states and is, therefore, neglected. Thus, the fit shown in Fig. 10 contains only temperature-dependence contributions from real critical spanning vectors.

The same fit is also shown in a 3D plot in Fig. 11. This 3D plot gives a better visualization of how the temperature dependence changes with spacer layer thickness. The
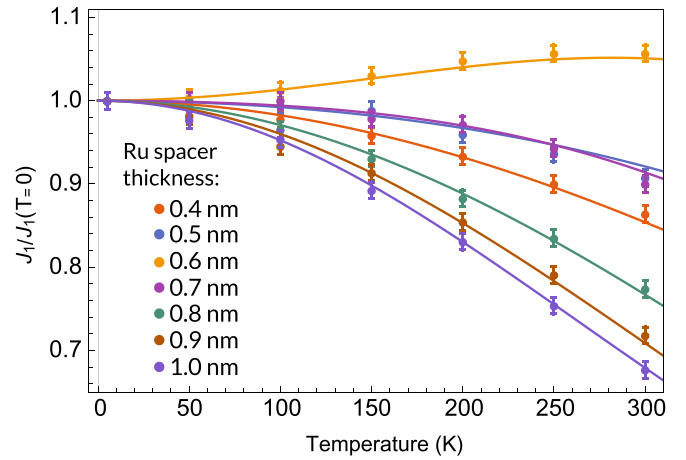
FIG. 10. J_1 temperature dependence for the Co/Ru/Co series with spacer layer thickness ranging from 0.4 to 1 nm and temperatures from 5 to 300 K, normalized to the zero-temperature J_1. The circles are experimental data, and the lines are fits using Eq. (14). The fits were performed on all measurements simultaneously so that each fit has the same parameters. The colors corresponding to spacer layer thicknesses are shown in the figure. See Fig. 11 for a three-dimensional (3D) image of the fit.

$v_\perp^\alpha$ and D_ϕ^α parameters obtained from the fit are shown in Table II.

The $v_\perp^\alpha$ values shown in Table II obtained from fitting the J_1 temperature dependence agree within the approximate ranges as calculated by Gall [36] using density functional calculations and the projector-augmented wave method. Specifically, the critical spanning vectors a and b, which are located on the "inner electron star" in the 3D Fermi surface (which can be seen in the reference of Gall [36]), all have relatively low-$v_\perp^\alpha$ values within the range of 1.5-5 $\times 10^5$ m/s. The critical spanning vectors d, e, and h, which are located in the outer
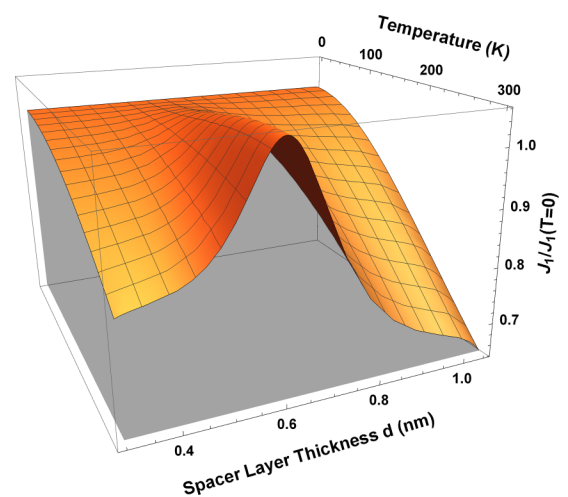
FIG. 11. A 3D plot of J_1 normalized to the zero-temperature value as described in Eq. (14) using parameters determined from fitting J_1 temperature-dependence data for the Co/Ru/Co series with spacer layer thickness ranging from 0.4 to 1 nm and temperatures from 5 to 300 K. This fit is the same fit shown in Fig. 10 except in 3D.

TABLE II. $v_\perp^\alpha$ and D_ϕ^α from Eq. (5) for each critical spanning vector as determined from fitting the temperature-dependence data in Fig. 10 using J^α values from Fig. 9 and bulk Ru critical spanning vectors listed in Table I with the exception of critical spanning vectors c and f because they were found to have an insignificant contribution to coupling.

CSV label	$v_\perp^\alpha \pm 0.6$ $(10^5$ m/s$)$	$D_\phi^\alpha \pm 0.5$ (eV^{-1})
a_1	4.8	3.1
a_2	1.7	0.0
b	2.9	4.1
d	8.0	6.4
e	6.0	5.4
g	9.8	0.0
h	15.9	6.6

"hole ring" in the 3D Fermi surface, have relatively large $v_\perp^\alpha$ values within the range of 6-16 $\times 10^5$ m/s. The h critical spanning vector from our fit has the largest $v_\perp^\alpha$, which is also in agreement with the calculations by Gall [36]. The relative differences of $v_\perp^\alpha$ between the critical spanning vectors are also in agreement with those calculated by Philip *et al.* [37] using the Perdew-Burke-Enzerhof generalized gradient approximation method.

The D_ϕ^α values shown in Table II obtained from fitting the J_1 temperature dependence have a wide range of values from 0 to 6.6 eV^{-1} depending on the critical spanning vector. These values are the same order of magnitude as the 2.4 eV^{-1} that Lee and Chang [24] found for Co/Cu/Co trilayer structures with (111)-oriented Cu, which only has one critical spanning vector, making it value a good indication of what to expect for each individual critical spanning vector. Additionally, Castro *et al.* [23] calculated using fully realistic tight-binding bands, a theoretical value of $D_\phi^\alpha = 4.53$ eV^{-1} for one of the critical spanning vectors in the Cu [001] direction for the Co/Cu/Co trilayer structure. This is also the same order of magnitude as the values obtained from our fit.

One large difference between our samples and that of Lee and Chang [24] is that instead of only having one critical spanning vector, we have seven. This means that for our samples, our fitting model has seven times more parameters than that of a Cu spacer layer growing along the [111] direction. This would allow our model to easily overfit any J_1 temperature dependence for a single spacer layer thickness or even a small number of spacer layer thicknesses. In order to mitigate this problem, we have measured the J_1 temperature dependence of seven different samples, all with different spacer layer thicknesses, and then simultaneously fit them all together. This provides more data so that there is less probability of an overfit and because the data are for different spacer layer thicknesses allow us to determine both temperature-dependence parameters. Specifically, we have 14 fitting parameters fit to 49 measurements. The fact that our fitted D_ϕ^α values for our individual critical spanning vectors are on the same order as those obtained from a single critical spanning vector show that our fit seems to be yielding reasonable results.

An important thing to note in Fig. 10 is that for the thinnest spacer layer of 0.4 nm, J_1 decreases with temperature. This is
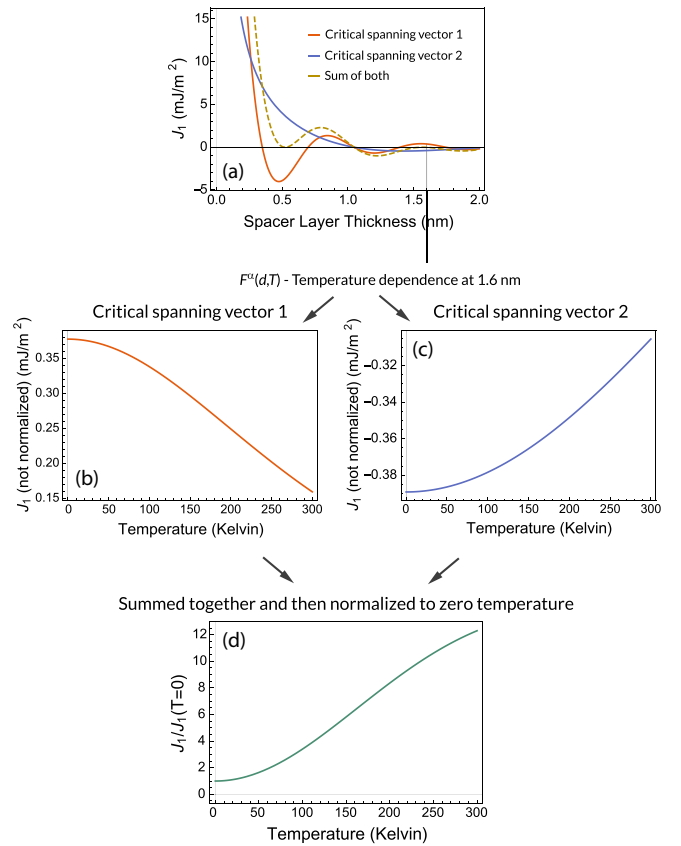
FIG. 12. (a) is J_1 for two different critical spanning vectors and the sum of them together, described by Eq. (2). (b) and (c) show the temperature dependence of each of the individual critical spanning vectors, described by Eq. (4) weighted by the value of J_1 at 1.6 nm for each critical spanning vector. (d) shows what would be the actual measured temperature dependence which is the sum of both contributions (normalized to the zero-temperature value after being added).

made visually obvious in the 3D plot in Fig. 11. If there was an exponential contribution to J_1 caused by evanescent electron states, it would dominate at the smallest spacer layer thickness and cause J_1 to increase with temperature. The fact that we do not see this is another strong indication that the nonoscillatory coupling seen in thinner Ru spacer layers is not an exponential contribution caused by evanescent electron states and is instead caused by a linear combination of contributions from oscillatory electron states.

The opposite temperature dependence of J_1 seen in the sample with a 0.6-nm thick spacer layer may look like an indication of contributions from evanescent states, but as you can see by the fit, it is well described without any evanescent states. This is because we have a linear combination of the temperature dependence of each of the critical spanning vectors weighted by their zero-temperature coupling strength, which is oscillating with spacer layer thickness. Depending on the thickness, some of these weighting factors will be positive, and some will be negative. This can lead to the temperature dependence being in the opposite direction for some critical spanning vectors relative to the others which can cause the opposite temperature dependence seen in our data. For illustrative purposes, we have shown a simulation of this taking place

for a system with only two critical spanning vectors, which is shown in Fig. 12. In this figure, critical spanning vector 1 has parameters $q_\perp^\alpha = 9$ nm^{-1}, $J^\alpha = 1$ mJ/m^2, $v_\perp^\alpha = 1 \times 10^5$ m/s, $D_\phi^\alpha = 0$ J^{-1}, $\phi^\alpha = 0$, and critical spanning vector 2 has parameters $q_\perp^\alpha = 3$ nm^{-1}, $J^\alpha = 1$ mJ/m^2, $v_\perp^\alpha = 2 \times 10^5$ m/s, $D_\phi^\alpha = 0$ J^{-1}, $\phi^\alpha = 0$. The temperature dependence was taken at $d = 1.6$ nm. (a) shows J_1 for the two critical spanning vectors and the sum of them together. (b) and (c) show the temperature dependence of each of the individual critical spanning vectors, described by Eq. (4) weighted by the value of J_1 at 1.6 nm for each critical spanning vector. (d) shows what would be the actual measured temperature dependence (normalized to its zero-temperature value). The main requirement for an inverted temperature dependence is that there are two or more critical spanning vectors with comparable J^α magnitudes but with opposite signs, which will occur periodically with spacer layer thickness for most spacer layers that have more than one dominant critical spanning vector.

The quality of the fit in Fig. 10 and the reasonable values of $v_\perp^\alpha$ and D_ϕ^α obtained from it indicate that the model appears to accurately represent the temperature dependence of J_1 that is occurring in our samples.

V. CONCLUSIONS

These results show that the bilinear interlayer exchange coupling in our Co/Ru/Co series of samples with additional data from the Pt/Co/Ru/Co series of samples is well described by the interface-reflection model including only

contributions from real critical spanning vectors obtained from bulk Ru.

The J^α values for each of the critical spanning vectors as determined from fitting thickness-dependent J_1 measurements, show that there are significant contributions to coupling from several different critical spanning vectors with different periods of oscillations. This indicates that bilinear interlayer exchange coupling cannot be characterized by only a single period of oscillations. This is in agreement with predictions performed by Stiles in Ref. [13].

By fitting spacer layer thickness and temperature-dependent J_1 measurements using the interface-reflection model, we have determined that there is likely no superexchangelike contribution to coupling. The nonoscillatory AFC bias of J_1 seen in thinner Ru spacer layers appears to be caused by a linear combination of oscillatory RKKY-like coupling from several different critical spanning vectors.

The fit to temperature-dependent J_1 measurements has resulted in $v_\perp^\alpha$ for each of the critical spanning vectors that are in approximate agreement with those calculated in Ref. [36]. The fit also resulted in D_ϕ^α values that are within the expected range as reported for similar experimental measurements and theoretical calculations. These results indicate that the temperature-dependence theory we have used appears to be capable of describing our J_1 measurements.

These results also show that, at least, for cobalt layers coupled across a Ru spacer layer, this model is able to describe bilinear interlayer exchange coupling with spacer layers as thin as 0.4 nm to a reasonable level of accuracy. This is despite using a theory that is only exact for infinitely thick spacer layers.

[1] P. Grünberg, R. Schreiber, Y. Pang, M. B. Brodsky, and H. Sowers, Phys. Rev. Lett. **57**, 2442 (1986).

[2] S. S. P. Parkin, N. More, and K. P. Roche, Phys. Rev. Lett. **64**, 2304 (1990).

[3] K. Yakushiji, A. Fukushima, H. Kubota, M. Konoto, and S. Yuasa, Appl. Phys. Express **6**, 113006 (2013).

[4] T. Devolder, S. Couet, J. Swerts, E. Liu, T. Lin, S. Mertens, A. Furnemont, and G. Kar, J. Appl. Phys. **121**, 113904 (2017).

[5] M. Cubukcu, O. Boulle, N. Mikuszeit, C. Hamelin, T. Brächer, N. Lamard, M. Cyrille, L. Buda-Prejbeanu, K. Garello, I. M. Miron, O. Klein, G. de Loubens, V. V. Naletov, J. Langer, B. Ocker, P. Gambardella, and G. Gaudin, IEEE Trans. Magn. **54**, 1 (2018).

[6] T. McKinnon, R. Hübner, B. Heinrich, and E. Girt, J. Appl. Phys. **127**, 053902 (2020).

[7] T. McKinnon and E. Girt, Appl. Phys. Lett. **113**, 192407 (2018).

[8] P. Bruno and C. Chappert, Phys. Rev. B **46**, 261 (1992).

[9] D. M. Edwards, J. Mathon, R. B. Muniz, and M. S. Phan, Phys. Rev. Lett. **67**, 493 (1991).

[10] J. Cullen and K. Hathaway, J. Appl. Phys. **70**, 5879 (1991).

[11] K. B. Hathaway and J. R. Cullen, J. Magn. Magn. Mater. **104**, 1840 (1992).

[12] R. P. Erickson, K. B. Hathaway, and J. R. Cullen, Phys. Rev. B **47**, 2626 (1993).

[13] M. D. Stiles, Phys. Rev. B **48**, 7238 (1993).

[14] P. Bruno, Phys. Rev. B **52**, 411 (1995).

[15] M. D. Stiles, Contemp. Concepts Condens. Matter Sci. **1**, 51 (2006).

[16] S. S. P. Parkin and D. Mauri, Phys. Rev. B **44**, 7131(R) (1991).

[17] J. Fassbender, F. Nörtemann, R. Stamps, R. Camley, B. Hillebrands, G. Güntherodt, and S. Parkin, J. Magn. Magn. Mater. **121**, 270 (1993).

[18] U. Ebels, R. L. Stamps, L. Zhou, P. E. Wigen, K. Ounadjela, J. Gregg, J. Morkowski, and A. Szajek, Phys. Rev. B **58**, 6367 (1998).

[19] P. Wigen, L. Zhou, R. Stamps, K. Ounadjela, M. Hehn, and J. Gregg, J. Magn. Magn. Mater. **165**, 465 (1997).

[20] S. Toscano, B. Briner, and M. Landolt, *Magnetism and Structure in Systems of Reduced Dimension* (Springer, Berlin, 1993), pp. 257–268.

[21] B. Heinrich and J. Cochran, Adv. Phys. **42**, 523 (1993).

[22] B. Khodadadi, J. B. Mohammadi, J. M. Jones, A. Srivastava, C. Mewes, T. Mewes, and C. Kaiser, Phys. Rev. Appl. **8**, 014024 (2017).

[23] J. d'Albuquerquee e Castro, J. Mathon, M. Villeret, and A. Umerski, Phys. Rev. B **53**, R13306(R) (1996).

[24] B. C. Lee and Y.-C. Chang, Phys. Rev. B **62**, 3888 (2000).

[25] S. Schwieger and W. Nolting, Phys. Rev. B **69**, 224413 (2004).

[26] N. W. Ashcroft and N. David Mermin, *Solid State Physics* (Holt, Rinehart and Winston, New York, 1976).

[27] P. Bruno, Phys. Rev. B **49**, 13231 (1994).

[28] P. Coleridge, J. Low Temp. Phys. **1**, 577 (1969).

[29] O. Jepsen, O. K. Andersen, and A. R. Mackintosh, Phys. Rev. B **12**, 3084 (1975).

[30] V. Romero-García, J. V. Sánchez-Pérez, S. Castiñeira-Ibáñez, and L. Garcia-Raffi, Appl. Phys. Lett. **96**, 124102 (2010).

[31] T. McKinnon, P. Omelchenko, B. Heinrich, and E. Girt, J. Appl. Phys. **123**, 223903 (2018).

[32] E. Girt and H. J. Richter, IEEE Trans. Magn. **39**, 2306 (2003).

[33] T. McKinnon, Study of magnetic interlayer coupling in synthetic antiferromagnets for use in MRAM devices, Ph.D. thesis, Simon Fraser University, 2020, https://summit.sfu.ca/item/21192.

[34] C. Eyrich, A. Zamani, W. Huttema, M. Arora, D. Harrison, F. Rashidi, D. Broun, B. Heinrich, O. Mryasov, M. Ahlberg, O. Karis, P. E. Jönsson, M. From, X. Zhu, and E. Girt, Phys. Rev. B **90**, 235408 (2014).

[35] G. Parker, *Guide-Wave Optical Communications: Materials* (Elsevier, Amsterdam, 2001), pp. 3703–3707.

[36] D. Gall, J. Appl. Phys. **119**, 085101 (2016).

[37] T. M. Philip, N. A. Lanzillo, T. Gunst, T. Markussen, J. Cobb, S. Aboud, and R. R. Robison, Phys. Rev. Appl. **13**, 044045 (2020).